



HHS Public Access

Author manuscript

Neuroimage. Author manuscript; available in PMC 2019 June 01.

Author Manuscript

Author Manuscript

Author Manuscript

Author Manuscript

Published in final edited form as:

Neuroimage. 2018 June ; 173: 35–48. doi:10.1016/j.neuroimage.2018.01.088.

Computationally Optimized ECoG Stimulation with Local Safety Constraints

Seyhmus Guler¹, Moritz Dannhauer^{2,3}, Biel Roig-Solvas⁴, Alexis Gkogkidis^{5,6}, Rob Macleod^{2,3}, Tonio Ball^{5,6}, Jeffrey G Ojemann⁷, and Dana H Brooks^{2,4}

¹Computational Radiology Laboratory (CRL), Boston Children's Hospital and Harvard Medical School, Boston, MA, USA

²Center for Integrative Biomedical Computing (CIBC), University of Utah, Salt Lake City, UT, USA

³Scientific Computing Institute (SCI), University of Utah, Salt Lake City, UT, USA

⁴B-SPIRAL Group, Department of Electrical and Computer Engineering, Northeastern University, Boston, MA, USA

⁵Intracranial EEG and Brain Imaging Lab, Epilepsy Center, University Hospital Freiburg, Freiburg, Germany

⁶BrainLinks-BrainTools Cluster of Excellence and Bernstein Center Freiburg, University of Freiburg, Freiburg, Germany

⁷Department of Neurological Surgery and the Center for Sensorimotor Neural Engineering, University of Washington, Seattle, WA, USA

Abstract

Direct stimulation of the cortical surface is used clinically for cortical mapping and modulation of local activity. Future applications of cortical modulation and brain-computer interfaces may also use cortical stimulation methods. One common method to deliver current is through electrocorticography (ECoG) stimulation in which a dense array of electrodes are placed subdurally or epidurally to stimulate the cortex. However, proximity to cortical tissue limits the amount of current that can be delivered safely. It may be desirable to deliver higher current to a specific local region of interest (ROI) while limiting current to other local areas more stringently than is guaranteed by global safety limits. Two commonly used global safety constraints bound the total injected current and individual electrode currents. However, these two sets of constraints may not be sufficient to prevent high current density locally (hot-spots). In this work, we propose an efficient approach that prevents current density hot-spots in the entire brain while optimizing ECoG stimulus patterns for targeted stimulation. Specifically, we maximize the current along a particular desired directional field in the ROI while respecting three safety constraints: one on the total injected current, one on individual electrode currents, and the third on the local current density magnitude in the brain. This third set of constraints creates a computational barrier due to the huge number of constraints needed to bound the current density at every point in the entire brain. We overcome this barrier by adopting an efficient two-step approach. In the first step, the

Corresponding author: Seyhmus Guler, seyhmus.guler@childrens.harvard.edu.

Author Manuscript
Author Manuscript
Author Manuscript
Author Manuscript

proposed method identifies the safe brain region, which cannot contain any hot-spots solely based on the global bounds on total injected current and individual electrode currents. In the second step, the proposed algorithm iteratively adjusts the stimulus pattern to arrive at a solution that exhibits no hot-spots in the remaining brain. We report on simulations on a realistic finite element (FE) head model with five anatomical ROIs and two desired directional fields. We also report on the effect of ROI depth and desired directional field on the focality of the stimulation. Finally, we provide an analysis of optimization runtime as a function of different safety and modeling parameters. Our results suggest that optimized stimulus patterns tend to differ from those used in clinical practice.

Keywords

ECoG; electrocorticography stimulation; optimization; safety; optimized; local safety constraints

1. Introduction

ECoG uses electrode arrays surgically implanted on the cortical surface. ECoG arrays are primarily used to localize seizure onset in patients with intractable epilepsy and to localize brain function (e.g., motor and language) to guide surgical resection [1], [2]. Stimulation through ECoG electrode arrays, typically through a bipolar electrode stimulation configuration, is done to target an underlying region of interest (ROI) which requires specificity of current delivery [3]. ECoG stimulation is used clinically as a therapeutic tool in an attempt to reduce seizures [4], neuropathic pain [5], to support recovery and plasticity in stroke in primates [6] and humans [7], and to provide sensory feedback for bidirectional brain-computer interfaces [8], [9]. These stimulation applications all require focal delivery of current to a specified ROI. Thus in addition to limitations fixed by safety consideration to avoid tissue injury, undesired but avoidable current delivered outside the ROI would limit flexibility of application.

ECoG stimulation can provide improved spatial specificity compared to scalp electrodes since the stimulation electrodes are placed directly on the cortical surface [10]. Proximity of the electrodes to the cortex, without the intervening attenuation from the skull and blurring from the full cerebrospinal fluid (CSF) layer, suggests enhanced ability to control currents across the grid to provide much more precise targeting of ROIs within the tissue. However, placing the electrodes directly on the cortical surface increases safety concerns since the proximity of electrodes to brain tissue also means unsafe current density could easily be delivered to active brain tissue [11]. Thus, there is a need for algorithms to design stimulus patterns for safe and effective current delivery to the ROI. In this work, we address this issue by proposing an optimization method to find a subject- and ROI-specific ECoG current injection pattern that maximizes the directional current in the ROI while satisfying constraints regarding subject safety, specifically in terms of bounding local current density everywhere in the brain.

To the best of our knowledge, the literature on optimization of electrode stimulus patterns for cortical stimulation is scarce. Kim and colleagues used computational models to

Author Manuscript
Author Manuscript
Author Manuscript
Author Manuscript

investigate the influence of certain stimulation and modeling parameters such as stimulation amplitudes, electrode configuration, and white matter conductivity specifications [10], [12]. Numerous methods to localize subdural electrodes have been proposed by Pieters and colleagues [13] but the authors considered only measurement electrodes and did not introduce methods to apply and optimize stimulation from the same set of electrodes. In contrast, several previous studies have proposed and solved analogous optimization problems for targeted transcranial stimulation using scalp electrodes [14]–[20]. In [20], Wagner and colleagues provide an in-depth analysis of mathematical models for multi-electrode tCS optimization, which they solve using an ADMM approach while ensuring subject safety via global and local constraints. Our work here starts from a method designed to optimize transcranial stimulation, but includes a novel approach to allow constraints on local current density while retaining computational efficiency.

Specifically, in these previous reports, two constraints were typically considered to protect subject safety; both the total injected current and all individual electrode currents were bounded by predefined limits [21]. In [19], our group introduced a third constraint, on the total current magnitude in the brain outside the ROI, allowing us to directly maximize directional current in the ROI with a well-specified constraint. We compared our approach with several others in the literature, as well as providing freely available software implementations of all approaches we studied [19]. However as we have already emphasized, these three safety constraints may not be sufficient in the case of ECoG stimulation. There is still a concern that optimized patterns will cause local current density maxima that exceed a desirable threshold and potentially harm the subject. We will refer to such undesirable maxima as “hot-spots” in what follows.

In this work we propose and test an efficient extension of our existing algorithm to optimize targeting of ROIs with ECoG stimulation, adding safety constraints to prevent such hot-spots across the entire brain. Specifically, the proposed algorithm maximizes the current density along a user-defined directional field in a user-defined cortical ROI while satisfying three safety constraints: (1) on the total injected current, (2) on individual electrode currents, and (3) on the local current density magnitude everywhere in the brain. We note that this approach shares the same objective function and first two safety constraints with our original optimization approach for scalp electrodes [19]. The third set of constraints, on the local current density magnitude in the brain, was added in response to the additional concerns raised when using ECoG arrays.

The main barrier to be addressed in this work is the computational complexity imposed by this new family of constraints, which we call “hot-spot constraints”. A straightforward approach would be to simply impose an additional hot-spot constraint for each small region in the brain. However achieving reasonable locality of these constraints, say on the order of 1 mm^3 volumes, would require checking millions of constraints. This makes this naive approach unscalable. Instead, we describe here a novel and efficient two-step approach that selectively adds hot-spot constraints. In the first step we use simple bounds based on the first two safety constraints (i.e. the safety constraints imposed on the total injected current and individual electrode currents) to identify a *safe* brain region that cannot contain hot-spots as long as those two constraints are satisfied. It turns out that this step typically reduces the

total number of hot-spot constraints by about two orders of magnitude. However this still leaves too many hotspot constraints to be computationally tractable, so in our second step we apply an iterative approach that selectively adds constraints in an efficient manner and is guaranteed to converge to an optimal solution. This second step typically reduces the original problem to one with at most a few thousand constraints, enabling us to compute the optimal ECoG stimulus patterns within seconds on a modern computer.

We report on tests of our method using simulations based on a realistic finite element (FE) head model with five anatomical cortical ROIs and two desired directional fields for each ROI. We assess the effect of ROI depth, desired directional field, and the threshold value for maximum allowable current density magnitude in the brain on the optimal patterns as well as on the convergence rate of the proposed optimization algorithm.

One interesting result from our simulations is that the resulting optimal stimulus patterns generally differ considerably from the “standard” bipolar (i.e. adjacent pair of electrodes from the ECoG grid) and monopolar (i.e. one electrode from the ECoG grid with a distant reference electrode used as the return) configurations used in clinical practice [22], [23], which suggests that the proposed method may have the potential to increase the capabilities of ECoG stimulation. The optimal stimulus patterns also appear to be sensitive to the anatomy of cortical folding patterns directly under the array, making prediction of optimal patterns without a sophisticated optimization method rather difficult.

The rest of the paper is organized as follows. In Section 2, we describe the proposed optimization approach in detail followed by a description of the simulation setup. Section 3 reports on our analysis of safe brain region, presents an exemplary optimization result for one of the ROIs, and then summarizes the optimization results for all five ROIs. In Section 4, we discuss our findings and potential future directions. We provide detailed results for all five ROIs in Appendix.

2. Methods

In this section, we first give an in-depth description of the optimization approach we devised. We introduce the objective function and the three sets of constraints employed to ensure subject safety. We then provide details of our two-step approach, outlined above, to solve this optimization problem. We conclude this section by describing the computer simulations we carried out to evaluate our method along with some details about the computational head model we employed.

2.1. Optimization problem

The objective function and first two constraints we adopt here are identical to those used in our previous work on transcranial stimulation [19] and we reprise them here only briefly. Specifically, the objective function is defined as the current density along a predefined desired directional field \mathbf{e} in the ROI [19]:

$$\max_{\mathbf{I}} \int_{\Omega_{ROI}} (\mathbf{J}(\mathbf{r}) \cdot \mathbf{e}(\mathbf{r})) d\mathbf{r}, \quad (1)$$

where \mathbf{J} represents the current density, \mathbf{e} denotes the desired directional field with unit magnitude, Ω_{ROI} stands for the ROI volume, \mathbf{I} is the array (organized as an $L \times 1$ column vector, L being the total number of electrodes) of electrode currents to be determined by the optimization, \mathbf{r} is the position vector, and \cdot is the vector dot product. We direct the reader to [19] for a detailed comparison between this choice of the objective function and two other choices frequently encountered in transcranial brain stimulation optimization.

The first two safety constraints imposed on the total injected current, and on each individual electrode current are formulated as [19]:

$$\|\mathbf{I}\|_1 \leq s_{tot} \quad (2a)$$

$$\|\mathbf{I}\|_\infty \leq s_{ind} \quad (2b)$$

where $\|\cdot\|_1$ denotes the 1-norm, and $\|\cdot\|_\infty$ is the infinity-norm. In words, (2a) ensures that the total current entering the head is bounded by s_{tot} , and (2b) ensures that each individual electrode current magnitude is bounded by s_{ind} .

The third set of safety constraints replaces the constraint on total current power in the brain outside the ROI that we used in our transcranial stimulation optimization in [19]. This set of constraints forces the current density magnitude in a set of arbitrarily small volumes in the brain, indexed here by p , to be below a pre-determined, and possibly location dependent, bound:

$$\|\mathbf{J}_p\|_2 \leq d_p \quad \forall p \in \Omega_{brain}, \quad (2c)$$

where $\|\cdot\|_2$ denotes the 2-norm, d_p is the threshold value for the current density magnitude in volume p in the brain, and Ω_{brain} represents the brain domain. Note that in our implementation we will take the elements to be finite element tetrahedra used in our calculations, but the formulation is more general here.

We note that the optimization problem introduced and solved by Wagner and colleagues in [20] for multi-electrode tCS targeting has several similarities and some important differences with the formulation presented here. First, the two objective functions are the same; the only difference between them is introduced in the development of [20] when additional Lagrangian terms are added. Second, the two methods share constraints on the total injected current and local current density magnitude but our constraint on each individual electrode is

absent in [20]. Third and most importantly, the two groups take substantially different approaches to reformulate their corresponding optimization problems to solve them in a computationally tractable fashion. Wagner et al. introduce L1 and L2 regularization terms in their objective function to penalize high current levels at the electrodes and sparsify the solution, and then employ the alternating direction method of multipliers (ADMM) to solve for the electrode current values after selection of Lagrange multipliers and other hyperparameters. In contrast, we employ a two-step approach where we first remove a subset of redundant hot-spot constraints using an upper bound analysis on the current density and then apply an iterative approach to solve the reduced problem in a computationally efficient manner. Thus two approaches differ in terms of computational complexity and how the optimization is handled at the implementation level.

In order to solve the optimization problem in (1) and (2), the transfer function between the current density \mathbf{J} and electrode current array \mathbf{I} needs to be known. As in [19], we use a linear finite element (FE) solver applied on a realistic head model to find this relationship. In our FE model, the head domain is discretized into small volume elements and the current density of the m 'th volume element¹ is approximated as a linear function of the potential at the nodes of that element, which we can then write as a linear function of the electrode current array:

$$\mathbf{J}_m = \mathbf{A}_m \mathbf{I}. \quad (3)$$

\mathbf{A}_m is a $3 \times L$ matrix, which represents a subset of the FE solution that maps the array of currents injected through the electrodes to the current density of m 'th volume element. The constraint (2c) can then be represented with a finite set of constraints on the brain volume elements:

$$\|\mathbf{J}_m\|_2 \leq d_m \quad \forall m \in \Omega_{\text{brain}}^{\text{discretized}}. \quad (4)$$

For a realistically discretized human head, the number of volume elements in the brain is usually on the order of tens of millions. Thus, as already noted, imposing (4) directly will introduce an intractable computational burden. However, it seems reasonable to expect that this constraint may be redundant for volume elements sufficiently far (electrically) from the ECoG electrodes. Based on this intuition, we developed a set of bounds to quickly identify and eliminate a large majority of those redundancies, using the head model and the first two constraints (2a) and (2b). Specifically we calculate mathematical upper bounds on the current density magnitude anywhere in the brain, as we describe next.

2.2. Removing redundant hot-spot constraints

For each m 'th volume element in the brain, we calculate four different upper bounds on the current density magnitude based on safety constraint bounds s_{tol} and s_{ind} , using the

¹We emphasize that we are using a discrete array of volume elements and replace p in (2c) with a finite element index m .

appropriate subset of the head model in (3). These four upper bounds are (see Appendix A for details):

$$U1: \|\mathbf{J}_m\|_2 \leq 2\|\mathbf{A}_m\|_1 s_{tot} \quad (5a)$$

$$U2: \|\mathbf{J}_m\|_2 \leq \sqrt{3}\|\mathbf{A}_m\|_\infty s_{ind} \quad (5b)$$

$$U3: \|\mathbf{J}_m\|_2 \leq 2\|\mathbf{A}_m\|_2 s_{tot} \quad (5c)$$

$$U4: \|\mathbf{J}_m\|_2 \leq \sqrt{L}\|\mathbf{A}_m\|_2 s_{ind} \quad (5d)$$

where the norms on the right hand side of the inequalities are induced matrix norms.

Based on these bounds we can easily check if the threshold value d_m at a particular brain volume element m is higher than *any* of these four upper bounds U1-4. If it is, we conclude that under these conditions (under the assumptions of the head model and for the specified safety constraint bounds s_{tot} and s_{ind}) it is mathematically impossible for the current density of that particular brain element to exceed d_m for any feasible current injection pattern. Thus, we do not need to explicitly impose (4) on that element as it is already guaranteed to meet that constraint. Note that it is sufficient for an element to have *any* of its respective four upper bounds, which depend on its particular relationship to the current-injecting electrodes, be smaller than d_m for it to be safe, even if it does not satisfy the other bounds. Thus the overall safe region is the union of safe regions determined by each bound separately. We identify the elements in the remaining brain region, which we will call *critical* region in the sequel, and pass them on to step two of the algorithm, which we describe next.

2.3. Iterative approach to solve the reduced problem

Even though a large majority of volume elements can be determined to be safe using the upper bounds described above (in our experiments we reduced the number of elements needing explicit handling by around two orders of magnitude), we are typically left with hundreds of thousands of hot-spot constraints for the remaining critical region, too many to be tractable to impose jointly. Thus, we devised an iterative approach in which at each iteration we select a subset of hotspot constraints that are violated in the previous iteration, reoptimize with those constraints added, and repeat the process until the added hot-spot constraint set is sufficient to prevent the occurrence of hot-spots in the entire critical region.

To start, an initial solution is found using solely the two safety constraints (2a) and (2b). At each succeeding iteration, the algorithm checks the feasibility of the current solution with

respect to the hot-spot constraints (4), and selects some of the violated hot-spot constraints to add to the current optimization problem if there are elements where that constraint is violated. The optimization is then carried out with the expanded constraint set and the process is repeated. The algorithm terminates once a solution that satisfies all the hot-spot constraints on all volume elements is reached. The termination of the algorithm is guaranteed, in a worst case scenario, after each mesh element in the critical region is constrained, but our experience is that many fewer constraints are needed to find a feasible solution.

The pseudo-code for this iterative approach is provided in Algorithm 1, with the notation explained below in Table I:

Algorithm 1

Iterative approach to find stimulus pattern with no hot-spots in the critical region.

```

 $C \leftarrow \emptyset$ 
Solve  $OP(C)$ 
 $H \leftarrow$  Violated hot-spot constraints
while  $H \neq \emptyset$  do
     $H_s \leftarrow$  A non-empty subset of  $H$ 
     $C \leftarrow C \cup H_s$ 
    Solve  $OP(C)$ 
     $H \leftarrow$  Violated hot-spot constraints
end while

```

To solve $OP(C)$ at each iteration of Algorithm 1 we use CVX, a package for specifying and solving convex programs [24], [25]. We note that $OP(C)$ has a global and unique optimal solution at each iteration², which allows us to solve the problem using a generic convex optimization solver. After an optimal solution is found, the current density magnitude in the critical region is computed to find all or a subset of the violated hot-spot constraints. In order to further speed up the algorithm, at intermediate iterations the algorithm only checks part of the critical region to choose a subset of violated hot-spot constraints and advance to the next iteration. In particular, it calculates the current density magnitude only for the elements on the cortical surface of the critical region. Once a solution that creates no hot-spots on the cortical surface of the critical region is found, it then proceeds to calculate the current density in the entire critical region at subsequent iterations, to identify hot-spots that might still occur in the volume. If there are such hot-spots, they are added as constraints in the next iteration, and if not, the algorithm terminates.

2.4. Simulation setup

In our simulations, we used a realistic head model with eight modeled tissue layers (scalp, skull, cerebrospinal fluid (CSF), gray matter (GM), white matter (WM), eye, internal air, and

² $OP(C)$ is a convex problem regardless of which brain volume elements are included in the hot-spot constraint set C . More specifically, the objective function in (1) becomes a linear function of electrode current array and the local hot-spot constraints in (4) turn into quadratic constraints after domain discretization [19].

insulating ECoG sheet), each assigned a scalar conductivity value [19]. A 6×8 ECoG grid with 1 cm inter-electrode distance was positioned on top of the left motor cortex, as shown in Figure 1. The head model was refined around the ECoG grid where the highest current density magnitude is most likely to occur. The electrodes were modeled as point electrodes represented by a set of FE mesh nodes.

We defined five anatomical ROIs with different depths, as shown in Figure 1. For each ROI, the *radial* desired directional field was based on the local cortical surface normal, and the *tangential* desired directional field was based on the plane tangential to the cortical surface³. The desired directional field clearly varies across the ROI volume due to the folded structure of the cortex however this change is smooth since the brain surface mesh itself was smoothed using a Laplacian filter. (We note that our definition of ‘radial’ and ‘tangential’ desired directional fields is based on the local structure of the cortex rather than the inner skull layer, which has been frequently used to define orientation in the source localization and non-invasive brain stimulation communities [17], [20], [26]–[28]).

The bound for the total injected current was set to 2 mA and individual electrode currents were bounded by 0.5 mA, for all cases, based on current levels reported in the literature [3]–[6]. The threshold for hot-spots was set to 2.5 A/m^2 for all brain elements outside the ROI. There were no constraints on the current density in the ROI, which rather was maximized along the desired directional field.

3. Results

Section A below reports on results on our analysis of safe and critical brain regions. Section B illustrates an exemplary optimization result for one of the ROIs with radial desired directional field. Section C presents summary results for all five cortical ROIs and two desired directions. In section D, we assess the effect of the threshold value for current density magnitude on the size of the critical region, as well as the optimal objective function value, and report on the runtime (computational time cost) of the algorithm for the simulations reported on here.

3.1. Safe vs. critical brain regions

Figure 2 shows safe and critical regions identified by each of the upper bounds U1–4 in (5), as well as the overall critical region determined by using all four bounds together. The gray color on each panel represents the safe brain region that cannot have current density magnitude higher than 2.5 A/m^2 , given that the total injected current is bounded by 2 mA and each individual electrode current is bounded by 0.5 mA. Thus, the green region is the critical brain region over which one needs to iteratively add hot-spot constraints to ensure its safety. It can be seen that different upper bounds identify different parts of the brain as safe; for example, the bound (2a) guarantees that frontal areas and almost the entire right hemisphere are below the specified safety threshold value, whereas the bound (2b) ensures that the region around the left posterior corner of the ECoG grid is below the threshold.

³There are infinitely many different vectors on the plane tangential to the cortical surface; here the vector with zero component in superior-inferior direction was chosen as the desired tangential directional field for each volume element.

Sulci and gyri beneath the grid are generally included in the critical region but not always gyral walls, a reflection of the difficulty of “steering” the current to gyral walls because of their orientation with respect to the ECoG grid. The unique contribution of each of the upper bounds on the safe region is summarized in Table II.

Overall, in this simulation and with the given electrode current limits and current density constraint, 97.10% of the entire brain was identified as safe using this upper bound analysis. The results show that for the given simulation setup, the bounds U1 and U2 had the dominant effect while the upper bound U3 did not contribute to defining the overall safe region as it was consistently larger than the bound U4. We note that the overall safe region is not equal to the sum of the four unique volumes identified by each bound because a significant part of the brain volume is identified as safe by more than one bound.

3.2. Exemplary results for one ROI with radial desired current direction

In this section we report on detailed results for one of the ROIs tested, and for the radial desired directional field. Results for all remaining cases are summarized in the sequel and included in detail in Appendix B. The ROI we report on is the one shown in purple in Figure 1, which we refer to as *gyral ROI* throughout the rest of the paper. In Figure 3 we visualize in detail the iteration-wise optimal stimulus patterns, the identified locations that violate the hot-spot constraint, and the corresponding current density fields. Each row corresponds to the results from one iteration. For each iteration the left column shows the critical area, the optimal stimulus pattern (mapped onto the electrode locations using the colormap shown) and the hot-spots found at tested locations. (Recall that we only test surface locations until those locations are all sufficiently constrained, and then include depth locations that still violate the constraint.) The middle column shows the current density magnitude on the cortical surface and indicates tested hot-spots highlighted with black contours. A thin white contour is drawn around the ROI to highlight its boundary; we kept this contour very thin not to block the current density magnitude visualization around the ROI. By imposing additional constraints on the hot-spots identified at previous iteration, the optimal current injection pattern shifts to employ other electrodes to prevent those hot-spots. This shift may in turn create new hot-spots, which if detected are then included in the constraint list in the next iteration. For this particular ROI and desired directional field, the algorithm terminates after iteration 4 as there are sufficient hot-spot constraints to prevent any hot-spot in the entire critical region. The number of detected hot-spots were 4047, 692, 178, and 0, at iterations 1, 2, 3, and 4, respectively. Note that since the ROI is excluded from the hot-spot constraints and the main goal is to maximize the directional current in the ROI, the current density in the ROI could be, and usually is, higher than the chosen threshold value. To illustrate the effect of different current injection pattern on volumetric current flow, the rightmost column in the figure visualizes current streamlines through the brain. We note that for these visualizations, all the seed points for the streamlines are chosen from the brain tissue, in order to visualize only some of the current that goes through the brain. Indeed, more current is shunted through the CSF than enters the brain tissue, but we chose this visualization method to avoid visual clutter. We observe from these visualizations that changing the current delivery patterns leverages the fact that the current passes more easily through CSF to “steer” the current and thus avoid hot-spots.

3.3. Summary of all the results for all ROIs

In order to assess the ability to affect the current flow in the ROI as a function of distance and desired directional field, we report the average current density along the desired orientation in the ROI as function of iteration in Figure 4 and the final values in Table III for more quantitative comparisons. We note that targeting ROI 2 (which is closer to the electrodes than ROI 3, 4, and 5) along the radial desired directional field is more difficult than targeting any of the other four remaining ROIs with respect to the same desired radial directional field. The average directional current density in the ROI drops with increasing depth for the other four ROIs. We also note that the average directional current density is not uniformly superior for one desired directional field than the other. These results suggest that the focality of the currents from a given stimulus pattern might depend on numerous factors such as specific anatomy, the electrode placement, the ROI depth, and the desired directional field.

Runtimes on a modern desktop computer (running Matlab code with no special attention to sophisticated efficiency methods) versus the total number of hot-spot constraints for all ROIs and all iterations are plotted in Figure 5. The figure suggests a linear relationship between runtime and number of constraints. We note that the runtime of a single iteration with about a thousand hot-spot constraints is in the range of a few seconds.

3.4. Effect of threshold value

To test the effect of the choice of safety threshold value we repeated the same set of calculations for four other thresholds. In Figure 6, we illustrate the five different critical regions found using the threshold values $d_m = 0.5, 1.5, 2.5, 3.5$, and 4.5 A/m^2 . The critical regions for these threshold values were determined to be 14.06%, 5.18%, 2.90%, 1.82%, and 1.15% of the entire brain volume, respectively.

If the critical region is larger in size, we would expect the optimization problem to take longer to solve as a bigger portion of the brain needs to be evaluated for hot-spots. Figure 7 shows the runtime as a function of the number of constraints for five critical region volumes derived from different threshold (d_m) values, for the gyral ROI and radial desired directional field. (Recall that we used the same ROI and desired directional field in section 3.2 to present exemplary results of our approach.) The runtime consistently increases with the size of the critical region and presumably as a consequence the average number of hot-spot constraints increases. Specifically, the number of hot-spot constraints and consequently the runtime in iterations for the case of $d_m = 0.5 \text{ A/m}^2$ are significantly higher than that of the other four cases.

Figure 8 shows the optimal objective function value at each iteration for all five threshold values, for above mentioned gyral ROI and radial desired directional field. Since there are no hot-spot constraints in the first iteration, the optimal objective function value is the same for all cases. Once the first set of hot-spot constraints are added at the 2nd iteration, an optimal value close to the final solution is obtained. The succeeding iterations manipulate the current injection pattern to eliminate hot-spots but barely influence the objective function value.

Note also that the difference between the objective function values for $d_m = 4.5 \text{ A/m}^2$ and $d_m = 3.5 \text{ A/m}^2$ is relatively low compared to other threshold pairs.

4. Discussion

In this computational study, we developed and solved an optimization problem to optimize stimulus patterns for ECoG stimulation, with the capability of preventing any local current density hot-spot in the entire brain. We introduced an efficient two-step approach that first identifies and discards unneeded hot-spot constraints in regions guaranteed to be below a safety threshold based on norm bounds derived from the global constraints, and then, iteratively adds hot-spot constraints on the remaining brain to further reduce the computation time. Our simulation results on a realistic head model showed that it is possible to prevent hot-spots across the entire brain, of course at the cost of reduced focality, directionality, and intensity in the target structures (Fig. 4).

Our results suggest that a significant portion of the brain tissue is not at risk of receiving high amplitude current density given that both total injected current and each individual electrode current are bounded. We also found that the complicated interactions among electrode locations, cortical folding, and conductivity differences (in particular the shunting effect of CSF) suggest that it may be possible to achieve non-obvious concentration of directional current in a chosen small ROI, while maintaining a bound on current outside that ROI even in adjacent areas, by utilizing electrode current patterns that can be determined by careful optimization. Our two-step computational approach, with the second step implemented in a greedy fashion to add hot-spot constraints iteratively, still finds fully feasible optimal solutions and allows the algorithm to run on standard hardware with no fine-tuned implementation required and with relatively small computational cost.

Our simulation results suggest that the optimal current stimulus patterns are dependent on many factors in addition to the ROI location with respect to cortical folds and electrode grid placement and anatomical details. These include the highest allowable current density magnitude in the brain and the desired direction for the current density in the ROI. It has also been shown that the type of the stimulation (voltage vs current controlled stimulation), electrode configuration (paddle-array vs single), the conductivity specifications of white matter (isotropic vs anisotropic) play a crucial role in the success of current delivery to the ROI [10]. Various *ad hoc* methods to localize electrode positions based on not only the visual cues but also the cortical structures have been proposed by Pieters and colleagues [13]. Moreover it is certainly feasible to design electrode arrays with electrode sizes, array pitch, and even shape/design of the electrodes themselves, different from the standard ECoG array modeled here [29]. Finally, optimal current stimulus patterns are typically not sparse due to hot-spot constraints. However sparse solutions could be achieved by additional constraints on the number of current sources or by introducing an L1 regularization term in the objective function [20], [30]. The complex interaction between all these design parameters and the head anatomy encourages computational models and sophisticated optimization methods even more.

We emphasize that the methods presented here could be directly extended to other brain stimulation modalities, e.g. to reduce localized high current densities on the scalp, and thus minimize discomfort (itching, tingling sensations) due to electrode edge effects⁴ [31] in transcranial current stimulation using large numbers of small scalp electrodes. Moreover, threshold values could be adjusted locally to maximize specificity of the stimulation, for example in an attempt to maximize the current in the hand area of the motor cortex with minimal current in the leg area. The approach could also be applied to different intracranial configurations such as depth electrodes or stereoEEG configurations [32], [33]. Similarly, the proposed method may also be applicable to prevent current density hotspots outside the desired volume of tissue activated (VTA) in multielectrode deep brain stimulation (DBS) applications [34].

In the work reported here, we used a common upper bound of 0.5 mA for each individual electrode current. This can be readily generalized to the case where each electrode current has its own upper and lower bound. In that case, the safety constraint in (2b) needs to be replaced with a safety constraint that allows for independently controlled lower and upper bounds on each individual electrode current:

$$\mathbf{I}^l \leq \mathbf{I} \leq \mathbf{I}^u, \quad (6)$$

where the operator ‘ \leq ’ stands for ‘element-wise less than or equal to’, \mathbf{I}^l and \mathbf{I}^u are the arrays of lower and upper bounds on individual electrode currents. We note that all the upper bounds in (5) are still valid if we simply replace s_{ind} with $\max(\|\mathbf{I}^l\|_\infty, \|\mathbf{I}^u\|_\infty)$ in (5b) and (5d).

The dose of a stimulation protocol is based on multiple factors, including the stimulation waveform (e.g. direct current (DC), alternating current (AC)) and duration. Since we use a quasi-static formulation with a resistive model of both tissue and electrodes, and only consider instantaneous current levels, waveform shape and duration did not play a role in our simulations. Optimizing for stimulus duration requires further assumptions about the stimulation waveform as well as tissue capacitance characteristics, which are beyond the scope of this report. If safety concerns require optimizing over stimulation duration as well, one possible direction would be to derive safety limits for the total injected charge, which is often considered as another safety metric along with the local current density magnitude [11], [35]–[37]. Since the total injected charge is a function of electrode currents, stimulation duration, and waveform, imposing a safety constraint on the total charge would also require these additional modeling steps. Charge constraints would effectively trade off stimulation duration for higher electrode current intensities. In any case, to the best of our knowledge it remains unclear how critical each metric is in terms of subject safety. In particular in the simulations reported on here we set the threshold current density magnitude to 2.5 A/m² based on the literature on safety limits for injected current density to prevent brain injury in transcranial stimulation [38].

⁴The current density is not uniformly distributed across the electrode-scalp interface and is larger at the electrode edges than in the center.

The approach we adopted here to reduce the total number of constraints is based on four upper bounds on the current density magnitude in the brain, which were derived from matrix and vector norm inequalities. These bounds are likely to be quite loose in practice. An alternative formulation, which would in principle achieve the highest feasible current density magnitude at a particular point in the brain, would be to formulate the entire problem as a constrained maximization. That is, instead of using possibly very loose upper bounds at each point, one could find the tightest upper bound for the current density magnitude via a maximization problem. This problem, however, is computationally challenging as it is non-convex, and guarantees of optimality could be difficult or impossible to obtain. Our bound approach performed satisfactorily in the work described here, in the sense that it generally allowed us to remove about 95% of the brain volume before engaging in iterative, and more expensive, FEM-based optimization calculations.

In a continuous domain, assuming that there are no interior current sources, Laplace's equation states that the divergence of the current density is zero at any interior volume point: $\nabla \cdot \mathbf{J} = 0$. This implies that the highest current density magnitude in a tissue layer occurs on the surface, not at an interior point. This encouraged us, at the implementation level, to check for, and prevent, hot-spots on the cortical surface first, and only after all the surface element constraints were satisfied search the remaining critical brain volume for potential hotspots. The need to also check the interior brain elements, despite the theoretical consideration just noted, is because errors due to discretization may produce unexpected effects and thus, although it is very unlikely, one might get a local hot-spot in the interior brain tissue rather than on the cortical surface solely due to the approximation errors in the head model. Thus to reduce the potential discrepancies between discrete model and continuous physical problem, we chose to add this additional step, which as we note had little added computational cost.

Perhaps the most important limitation, beyond those discussed above, has to do with potential impact of the head model on our results and conclusions. First, our isotropic head model was based on multimodal imaging data of a healthy subject and the ECoG sheet containing 48 nodal-based electrodes was registered onto the model via computer software. It is unclear how the craniotomy and the surgical procedure of planting cortical electrode grids on the cortex affects the model structurally and consequently the optimal stimulus patterns [39]; coregistration of preoperative and post-operative imaging data to generate accurate realistic head models is an on-going research topic [13], [39], [40]. We assigned scalar conductivity values to different tissue layers in the head model based on values reported in the literature; we note that it has been reported that different conductivity profiles for the head tissue could impact optimal stimulus patterns for transcranial stimulation [41]. Quantifying sensitivity to such model mismatch, as well as any compensatory algorithmic strategies that might be appropriate, is an important topic, and one that we are currently working on, but outside of the scope of this paper. Second, modeling of the dura mater and its thickness may change the current flow considerably depending upon whether the electrodes are placed epidurally or subdurally [10], [42], [43], and especially for the ROIs close to the inter hemispheric fissure, where the dura layer folds inside. Third, it has been reported that electrode number, size and shape might play an important role in the current

flow in the head [10], [44], which is not fully addressed in this work. We modeled the ECoG electrodes as point electrodes in our simulations here; however more sophisticated electrode models (e.g. the complete electrode model [45]) could be employed to more realistically represent the electrode-tissue boundary if that relationship is known; for example we used the complete electrode model for the tCS work reported in [19]. Different electrode models and their impact on the current flow in the head have previously been studied in various reports (e.g. [46]). Finally, the sulcus width has been reported to have significant effect on the induced electric field in the brain for transcranial magnetic stimulation [47] and this is also a topic of current research [48], [49]. We may have overestimated the sulcus width in our head model simply due to the resolution limits of the imaging, and consequently our results for targeting deep brain regions may be too optimistic. Finite element modeling of transcranial current stimulation has been validated with experimental measurements on the scalp [50], [51] and recently also with implanted electrodes [52]. To our knowledge there have not been any studies validating stimulation models with ECoG electrodes. There is no obvious technical reason beyond the geometric modeling difficulties noted above to expect the modeling to be more or less accurate than with transcranial stimulation; nonetheless validation against invasive experimental measurements is currently under way in our group.

Despite these modeling limitations, the main point of this paper was to present methodology that makes optimization of cortical electrode arrays with carefully chosen safety constraints possible. The methods presented here are essentially independent of the structural and volume conduction models and thus should be directly applicable to more complicated head and electrode models. In other words, increased simulation model complexity does not pose any concern in terms of the proposed algorithms converging in reasonable computation time to a (model-dependent) globally optimal current injection pattern that creates no local hot-spots in the brain tissue. However, we would like to reiterate here that optimal stimulus patterns might and most likely will differ from those reported here when different models and modeling parameters are used.

Finally, we firmly believe that the most critical need in terms of following up on this work is to validate our methodology with experimental measurements. We are actively pursuing such studies in phantoms, animal preparations, and humans.

5. Conclusion

This paper presents a novel and efficient approach to optimize stimulus pattern of ECoG electrode arrays, paying careful attention to the current density magnitude in the entire brain. The approach adopts a two-step algorithm to tackle the otherwise daunting problem of bounding the current density magnitude across the entire brain in a reasonably complex head model while optimizing the stimulus pattern for ECoG stimulation. We showed via computer simulations that both the ROI depth and the desired directional field are critical factors for both the amount of the directional current delivered to the ROIs and the optimal current pattern to apply, and the results seem to be sensitive to the bound imposed on the highest allowable current magnitude in the brain. We believe that the modeling and optimization methods presented here could help design stimulation protocols for many current, as well as emerging, cortical stimulation applications. In addition, these approaches could readily be

extended to the other brain stimulation modalities, both to identify the brain region that cannot contain hot-spots based on global safety constraints and also to prevent hot-spots in the remaining brain, the latter achieved by adapting our iterative optimization algorithm.

Acknowledgments

This study was supported in part by the NIH/NIGMS Center for Integrative Biomedical Computing, P41 GM103545 and by Joint US (NSF) German (DRG) Collaborative Research in Computational Neuroscience grant on Optimization of Human Cortical Stimulation, 1515168. We thank Dr. Don Tucker, Dr. Phan Luu, and Electrical Geodesics, Inc. (EGI) for generously providing multi-modal imaging data (CT, DTI, and MRI) used to generate realistic head model in our simulations.

References

1. Palmini A. The concept of the epileptogenic zone: a modern look at penfield and jaspers views on the role of interictal spikes. *Epileptic disorders*. 2006; 8(2):10–15.
2. Najm IM, Bingaman WE, Lüders HO. The use of subdural grids in the management of focal malformations due to abnormal cortical development. *Neurosurgery Clinics of North America*. 2002; 13(1):87–92. [PubMed: 11754319]
3. Schevon CA, Carlson C, Zaroff CM, Weiner HJ, Doyle WK, Miles D, Lajoie J, Kuzniecky R, Pacia S, Vazquez B, et al. Pediatric language mapping: sensitivity of neurostimulation and wada testing in epilepsy surgery. *Epilepsia*. 2007; 48(3):539–545. [PubMed: 17284300]
4. Morrell MJ. Responsive cortical stimulation for the treatment of medically intractable partial epilepsy. *Neurology*. 2011; 77(13):1295–1304. [PubMed: 21917777]
5. Meyerson, B., Lindblom, U., Linderoth, B., Lind, G., Herregodts, P. Advances in Stereotactic and Functional Neurosurgery. Vol. 10. Springer; 1993. Motor cortex stimulation as treatment of trigeminal neuropathic pain; p. 150-153.
6. Plow EB, Carey JR, Nudo RJ, Pascual-Leone A. Invasive cortical stimulation to promote recovery of function after stroke a critical appraisal. *Stroke*. 2009; 40(5):1926–1931. [PubMed: 19359643]
7. Balossier A, Etard O, Descat C, Vivien D, Emery E. Epidural cortical stimulation as a treatment for poststroke aphasia a systematic review of the literature and underlying neurophysiological mechanisms. *Neurorehabilitation and neural repair*. 2015 p. 1545968315606989.
8. Rothschild RM. Neuroengineering tools/applications for bidirectional interfaces, brain–computer interfaces, and neuroprosthetic implants—a review of recent progress. *Frontiers in neuroengineering*. 2010; 3:112. [PubMed: 21060801]
9. Collins KL, Guterstam A, Cronin J, Olson JD, Ehrsson HH, Ojemann JG. Ownership of an artificial limb induced by electrical brain stimulation. *Proceedings of the National Academy of Sciences*. 2016 p. 201616305.
10. Kim D, Seo H, Kim H-I, Jun SC. Computational study on subdural cortical stimulation—the influence of the head geometry, anisotropic conductivity, and electrode configuration. *PloS one*. 2014; 9(9):e108028. [PubMed: 25229673]
11. Merrill DR, Bikson M, Jefferys JG. Electrical stimulation of excitable tissue: design of efficacious and safe protocols. *Journal of neuroscience methods*. 2005; 141(2):171–198. [PubMed: 15661300]
12. Kim, D., Seo, H., Kim, H-I., Jun, SC. 2012 Annual International Conference of the IEEE Engineering in Medicine and Biology Society. IEEE; 2012. The computational study of subdural cortical stimulation: A quantitative analysis of voltage and current stimulation; p. 867-870.
13. Pieters TA, Conner CR, Tandon N. Recursive grid partitioning on a cortical surface model: an optimized technique for the localization of implanted subdural electrodes: Clinical article. *Journal of neurosurgery*. 2013; 118(5):1086–1097. [PubMed: 23495883]
14. Park J-H, Hong SB, Kim D-W, Suh M, Im C-H. A novel array-type transcranial direct current stimulation (tdcs) system for accurate focusing on targeted brain areas. *Magnetics, IEEE Transactions on*. 2011; 47(5):882–885.
15. Jung Y-J, Kim J-H, Kim D, Im C-H. An image-guided transcranial direct current stimulation system: a pilot phantom study. *Physiological measurement*. 2013; 34(8):937. [PubMed: 23897099]

16. Sadleir R, Vannorsdall T, Schretlen D, Gordon B. Target optimization in transcranial direct current stimulation. *Front Psychiatry*. 2012; 3:90. [PubMed: 23087654]
17. Dmochowski J, Datta A, Bikson M, Su Y, Parra L. Optimized multi-electrode stimulation increases focality and intensity at target. *J Neural Eng.* Aug. 2011; 8:046011. [PubMed: 21659696]
18. Ruffini G, Fox MD, Ripolles O, Miranda PC, Pascual-Leone A. Optimization of multifocal transcranial current stimulation for weighted cortical pattern targeting from realistic modeling of electric fields. *Neuroimage*. 2014; 89:216–225. [PubMed: 24345389]
19. Guler S, Dannhauer M, Erem B, Macleod R, Tucker D, Turovets S, Luu P, Erdogmus D, Brooks DH. Optimization of focality and direction in dense electrode array transcranial direct current stimulation (tdcs). *Journal of Neural Engineering*. 2016; 13(3):36020–36033.
20. Wagner S, Burger M, Wolters CH. An optimization approach for well-targeted transcranial direct current stimulation. *SIAM Journal on Applied Mathematics*. 2016; 76(6):2154–2174.
21. Fregni F, Nitsche M, Loo C, Brunoni A, Marangolo P, Leite J, Carvalho S, Bolognini N, Caumo W, Paik N, et al. Regulatory considerations for the clinical and research use of transcranial direct current stimulation (tdcs): Review and recommendations from an expert panel. *Clinical research and regulatory affairs*. 2015; 32(1):22–35. [PubMed: 25983531]
22. Kovac S, Scott CA, Maglajlija V, Toms N, Rodionov R, Miserocchi A, McEvoy AW, Diehl B. Comparison of bipolar versus monopolar extraoperative electrical cortical stimulation mapping in patients with focal epilepsy. *Clinical Neurophysiology*. 2014; 125(4):667–674. [PubMed: 24135067]
23. Kombos T, Suess O, Kern B-C, Funk T, Hoell T, Kopetsch O, Brock M. Comparison between monopolar and bipolar electrical stimulation of the motor cortex. *Acta neurochirurgica*. 1999; 141(12):1295–1301. [PubMed: 10672300]
24. Grant M, Boyd S, Ye Y. Cvx: Matlab software for disciplined convex programming. 2008
25. Grant, M., Boyd, S. Graph implementations for nonsmooth convex programs. In: Blondel, V.Boyd, S., Kimura, H., editors. Recent Advances in Learning and Control. Springer-Verlag Limited; 2008. p. 95-110.Lecture Notes in Control and Information Sciences http://stanford.edu/~boyd/graph_dcp.html
26. Whittingstall K, Stroink G, Gates L, Connolly J, Finley A. Effects of dipole position, orientation and noise on the accuracy of eeg source localization. *Biomedical engineering online*. 2003; 2(1): 14. [PubMed: 12807534]
27. Liu AK, Dale AM, Belliveau JW. Monte carlo simulation studies of eeg and meg localization accuracy. *Human brain mapping*. 2002; 16(1):47–62. [PubMed: 11870926]
28. Dannhauer M, Lämmel E, Wolters CH, Knösche TR. Spatiotemporal regularization in linear distributed source reconstruction from eeg/meg: a critical evaluation. *Brain topography*. 2013; 26(2):229–246. [PubMed: 23112100]
29. Wang X, Gkogkidis A, Ilijina O, Fiederer L, Henle C, Mader I, Kaminsky J, Stieglitz T, Gierthmuehlen M, Ball T. Mapping the fine structure of cortical activity with different micro-ecog electrode array geometries. *Journal of neural engineering*. 2017
30. Guler, S., Dannhauer, M., Erem, B., Macleod, R., Tucker, D., Turovets, S., Luu, P., Meleis, W., Brooks, D. 2016 IEEE International Symposium on Biomedical Imaging (ISBI). IEEE; 2016. Optimizing stimulus patterns for dense array tdcs with fewer sources than electrodes using a branch and bound algorithm.
31. Wagner T, Fregni F, Fecteau S, Grodzinsky A, Zahn M, Pascual-Leone A. Transcranial direct current stimulation: a computer-based human model study. *Neuroimage*. 2007; 35(3):1113–1124. [PubMed: 17337213]
32. Munari, C., Kahane, P., Tassi, L., Francione, S., Hoffmann, D., Russo, GL., Benabid, A. Advances in Stereotactic and Functional Neurosurgery. Vol. 10. Springer; 1993. Intracerebral low frequency electrical stimulation: a new tool for the definition of the epileptogenic area?; p. 181-185.
33. Hofmanis, J., Louis-Dorr, V., Cecchin, T., Caspary, O., Koessler, L. Engineering in Medicine and Biology Society, EMBC, 2011 Annual International Conference of the IEEE. IEEE; 2011. Propagation of electrical field in the brain using electrical intra-cerebral stimulations; p. 3888-3891.

34. Butson CR, Cooper SE, Henderson JM, McIntyre CC. Patient-specific analysis of the volume of tissue activated during deep brain stimulation. *Neuroimage*. 2007; 34(2):661–670. [PubMed: 17113789]
35. Nitsche MA, Liebetanz D, Lang N, Antal A, Tergau F, Paulus W. Safety criteria for transcranial direct current stimulation (tDCS) in humans. *Clinical Neurophysiology*. 2003; 114(11):2220–2222. [PubMed: 14580622]
36. McCreery DB, Agnew WF, Yuen TG, Bullara L. Charge density and charge per phase as cofactors in neural injury induced by electrical stimulation. *Biomedical Engineering, IEEE Transactions on*. 1990; 37(10):996–1001.
37. Brummer S, Turner M. Electrochemical considerations for safe electrical stimulation of the nervous system with platinum electrodes. *IEEE Transactions on Biomedical Engineering*. 1977; 24(1):59–63. [PubMed: 851475]
38. Bikson M, Grossman P, Thomas C, Zannou AL, Jiang J, Adnan T, Mourdoukoutas AP, Kronberg G, Truong D, Boggio P, et al. Safety of transcranial direct current stimulation: evidence based update 2016. *Brain Stimulation*. 2016; 9(5):641–661. [PubMed: 27372845]
39. Fiederer LDJ, Lahr J, Vorwerk J, Lucka F, Aertsen A, Wolters CH, Schulze-Bonhage A, Ball T. Electrical stimulation of the human cerebral cortex by extracranial muscle activity: Effect quantification with intracranial eeg and fMRI simulations. *IEEE Transactions on Biomedical Engineering*. 2016; 63(12):2552–2563. [PubMed: 27448334]
40. Zhang Y, Ding L, van Drongelen W, Hecox K, Frim DM, He B. A cortical potential imaging study from simultaneous extra- and intracranial electrical recordings by means of the finite element method. *NeuroImage*. 2006; 31(4):1513–1524. [PubMed: 16631381]
41. Schmidt C, Wagner S, Burger M, van Rienen U, Wolters CH. Impact of uncertain head tissue conductivity in the optimization of transcranial direct current stimulation for an auditory target. *Journal of neural engineering*. 2015; 12(4):046028. [PubMed: 26170066]
42. Manola L, Roelofsen B, Holsheimer J, Marani E, Geelen J. Modelling motor cortex stimulation for chronic pain control: electrical potential field, activating functions and responses of simple nerve fibre models. *Medical and biological engineering and computing*. 2005; 43(3):335–343. [PubMed: 16035221]
43. Wongsarnipagoon A, Grill WM. Computational modeling of epidural cortical stimulation. *Journal of neural engineering*. 2008; 5(4):443. [PubMed: 19015584]
44. Wei XF, Grill WM. Analysis of high-perimeter planar electrodes for efficient neural stimulation. *Frontiers in neuroengineering*. 2009; 2:15. [PubMed: 19936312]
45. Cheng K, Isaacson D, Newell J, Gisser D. Electrode models for electric current computed tomography. *IEEE Trans Biomed Eng*. Sep. 1989; 36:918–924. [PubMed: 2777280]
46. Pursiainen S, Agsten B, Wagner S, Wolters C. Advanced boundary electrode modeling for tES and parallel tES/eEG. *IEEE Transactions on Neural Systems and Rehabilitation Engineering*. 2017
47. Janssen A, Rampersad S, Lucka F, Lanfer B, Lew S, Aydin Ü, Wolters C, Stegeman D, Oostendorp T. The influence of sulcus width on simulated electric fields induced by transcranial magnetic stimulation. *Physics in medicine and biology*. 2013; 58(14):4881. [PubMed: 23787706]
48. Rampersad, S., Janssen, A. The influence of sulcus width on accuracy of tCS simulations; Abstract at Neuromodulation Conference; New York City, NY, USA. 2017;
49. Rampersad, S., Janssen, A. The influence of sulcus width on accuracy of tCS simulations; Abstract at Brain Stimulation and Imaging Meeting; Vancouver, Canada. 2017.
50. Datta A, Zhou X, Su Y, Parra LC, Bikson M. Validation of finite element model of transcranial electrical stimulation using scalp potentials: implications for clinical dose. *Journal of neural engineering*. 2013; 10(3):036018. [PubMed: 23649036]
51. Bangera NB, Schomer DL, Dehghani N, Ulbert I, Cash S, Papavasiliou S, Eisenberg SR, Dale AM, Halgren E. Experimental validation of the influence of white matter anisotropy on the intracranial eeg forward solution. *Journal of computational neuroscience*. 2010; 29(3):371–387. [PubMed: 20063051]
52. Huang Y, Liu AA, Lafon B, Friedman D, Dayan M, Wang X, Bikson M, Doyle WK, Devinsky O, Parra LC. Measurements and models of electric fields in the in vivo human brain during transcranial electric stimulation. *Elife*. 2017; 6:e18834. [PubMed: 28169833]

53. Golub, GH., Van Loan, CF. Matrix computations. Vol. 3. JHU Press; 2012.

Appendix A

Upper bounds on the current density magnitude in the brain

If \mathbf{A} is a matrix of size $M \times L$ and \mathbf{x} is a column vector of size $L \times 1$, then the following inequalities hold for any $\mathbf{A} \in \mathbb{R}^{M \times L}$, $\mathbf{x} \in \mathbb{R}^{L \times 1}$, and induced p-norm [53]:

$$\|\mathbf{Ax}\|_p \leq \|\mathbf{A}\|_p \|\mathbf{x}\|_p \quad (\text{A.1a})$$

$$\|\mathbf{x}\|_2 \leq \|\mathbf{x}\|_1 \quad (\text{A.1b})$$

$$\|\mathbf{x}\|_2 \leq \sqrt{L} \|\mathbf{x}\|_\infty \quad (\text{A.1c})$$

where $\|\cdot\|_p$ represents the (induced) p-norm, $\|\cdot\|_2$ the 2-norm, $\|\cdot\|_1$ the 1-norm, and $\|\cdot\|_\infty$ the infinity norm. Combining these inequalities with the two constraints (2a) and (2b) we calculate four different upper bounds on the current density magnitude at each volume element in the brain (note that the notation under the inequalities below refer to the equation number above that implies that step):

$$\text{U1: } \|\mathbf{J}_m\|_2 \stackrel{(\text{A.1b})}{\leq} \|\mathbf{J}_m\|_1 \stackrel{(\bar{3})}{=} \|\mathbf{A}_m \mathbf{I}\|_1 \stackrel{(\text{A.1a})}{\leq} \|\mathbf{A}_m\|_1 \|\mathbf{I}\|_1 \stackrel{(2a)}{\leq} 2 \|\mathbf{A}_m\|_1 s_{tot} \quad (\text{A.2a})$$

$$\text{U2: } \|\mathbf{J}_m\|_2 \stackrel{(\text{A.1c})}{\leq} \sqrt{3} \|\mathbf{J}_m\|_\infty \stackrel{(\bar{3})}{=} \sqrt{3} \|\mathbf{A}_m \mathbf{I}\|_\infty \stackrel{(\text{A.1a})}{\leq} \sqrt{3} \|\mathbf{A}_m\|_\infty \|\mathbf{I}\|_\infty \stackrel{(2b)}{\leq} \sqrt{3} \|\mathbf{A}_m\|_\infty s_{ind} \quad (\text{A.2b})$$

$$\text{U3: } \|\mathbf{J}_m\|_2 \stackrel{(\bar{3})}{=} \|\mathbf{A}_m \mathbf{I}\|_2 \stackrel{(\text{A.1a})}{\leq} \|\mathbf{A}_m\|_2 \|\mathbf{I}\|_2 \stackrel{(\text{A.1b})}{\leq} \|\mathbf{A}_m\|_2 \|\mathbf{I}\|_1 \stackrel{(2a)}{\leq} 2 \|\mathbf{A}_m\|_2 s_{tot} \quad (\text{A.2c})$$

$$\text{U4: } \|\mathbf{J}_m\|_2 \stackrel{(\bar{3})}{=} \|\mathbf{A}_m \mathbf{I}\|_2 \stackrel{(\text{A.1a})}{\leq} \|\mathbf{A}_m\|_2 \|\mathbf{I}\|_2 \stackrel{(\text{A.1c})}{\leq} \sqrt{L} \|\mathbf{A}_m\|_2 \|\mathbf{I}\|_\infty \stackrel{(2b)}{\leq} \sqrt{L} \|\mathbf{A}_m\|_2 s_{ind}. \quad (\text{A.2d})$$

Above, \mathbf{J}_m is a 3×1 column vector representing the current density of the m^{th} volume element, and \mathbf{A}_m denotes the $3 \times L$ matrix that maps, through the FE solutions, the $L \times 1$ electrode current array \mathbf{I} to the current density \mathbf{J}_m . We note that second upper bound U2 has a $\sqrt{3}$ term due to applying (A.1c) on the current density vector \mathbf{J}_m ($L = 3$). Also note that

fourth upper bound U_4 depends on the total number of electrodes, which we left as a free variable L after applying (A.1c) on the electrode current array \mathbf{I} .

Appendix B

All simulation results

We present optimization results for all five ROIs and both desired directional fields. Figures B.1, B.2, B.3, B.4, and B.5 present results for radial desired directional field and figures B.6, B.7, B.8, B.9, and B.10 for tangential desired directional field.

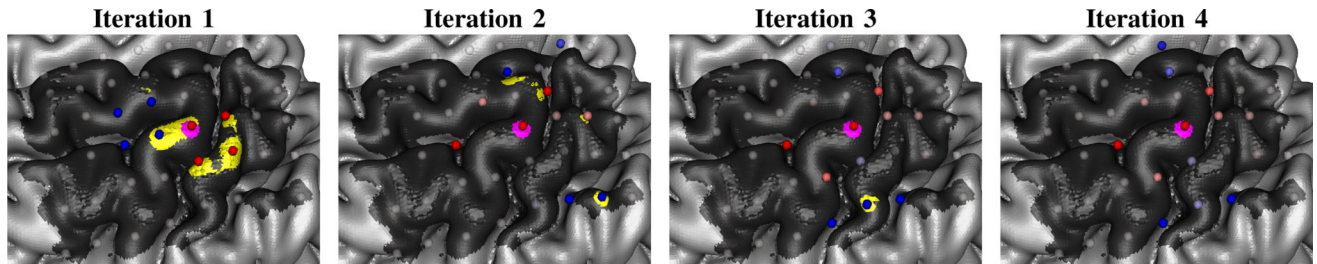


Fig. B.1.
Optimization results for ROI 1, in radial direction.

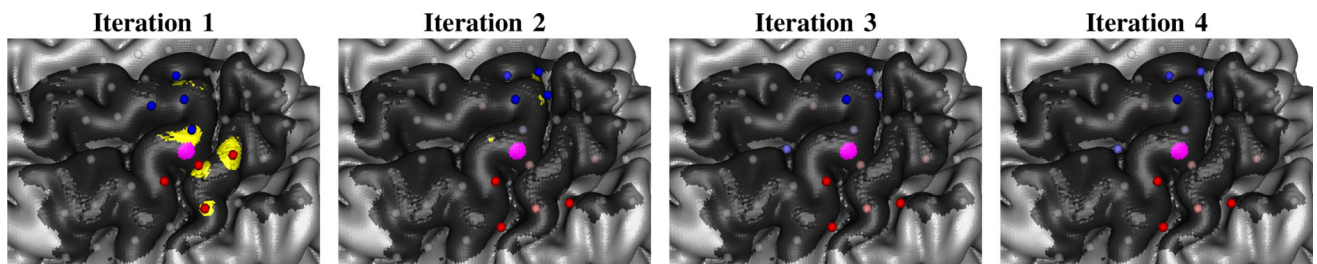


Fig. B.2.
Optimization results for ROI 2, in radial direction.

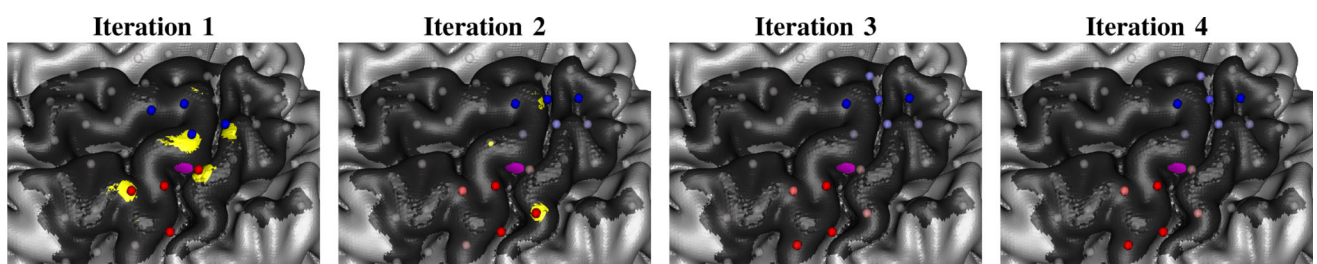


Fig. B.3.
Optimization results for ROI 3, in radial direction.

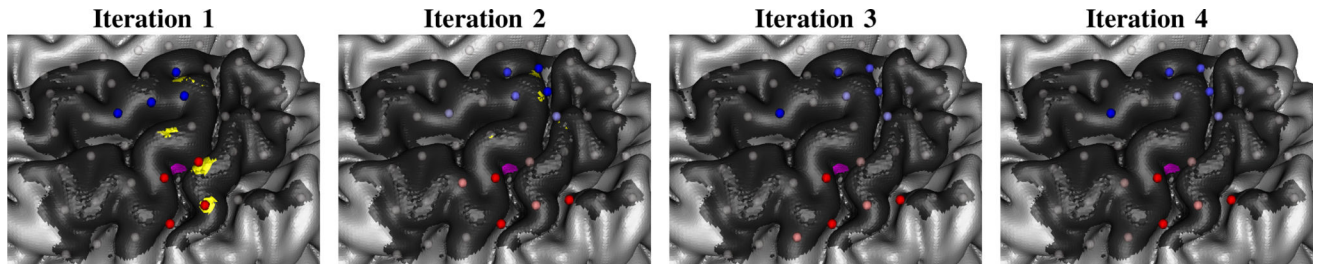


Fig. B.4.
Optimization results for ROI 4, in radial direction.

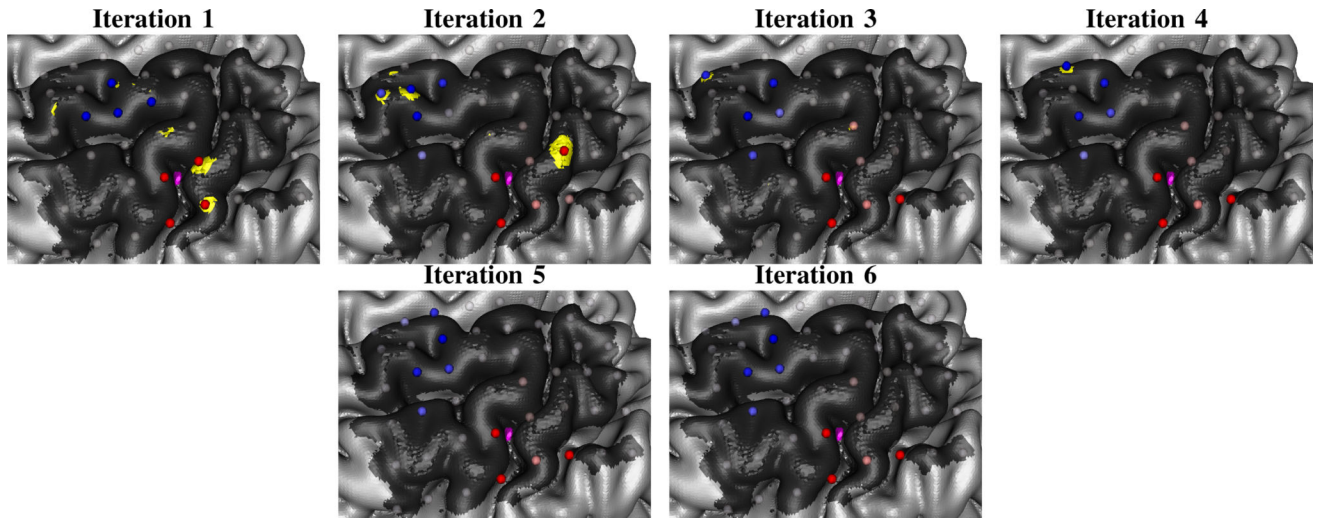


Fig. B.5.
Optimization results for ROI 5, in radial direction.

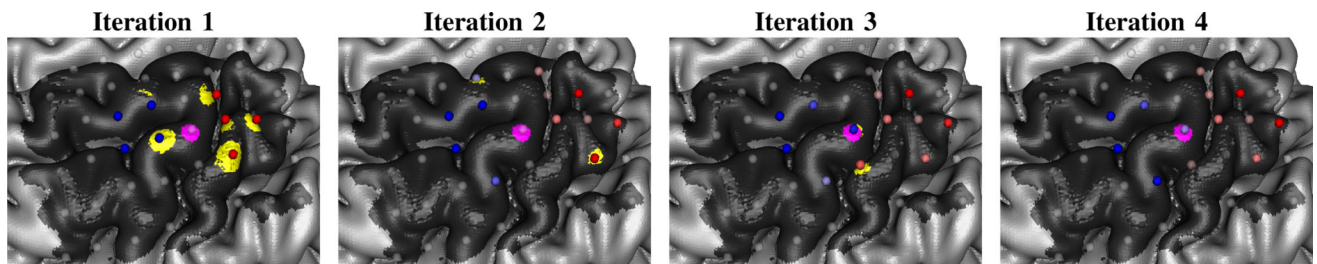


Fig. B.6.
Optimization results for ROI 1, in tangential direction.

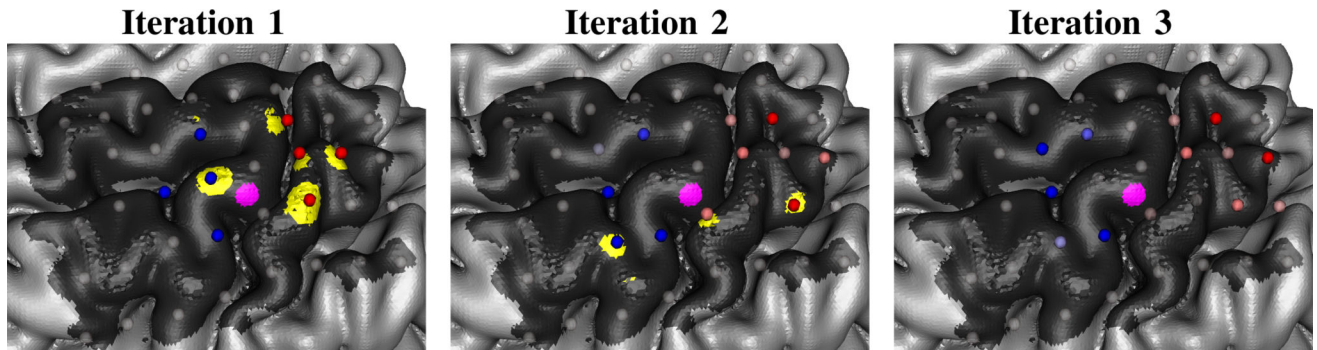


Fig. B.7.

Optimization results for ROI 2, in tangential direction.

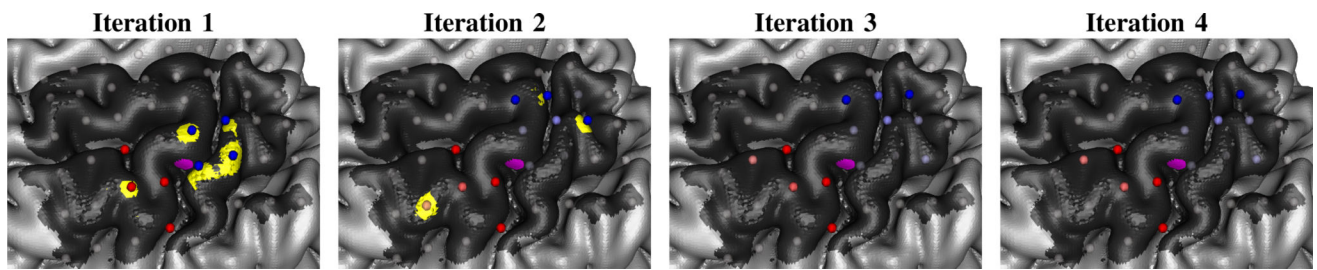


Fig. B.8.

Optimization results for ROI 3, in tangential direction.

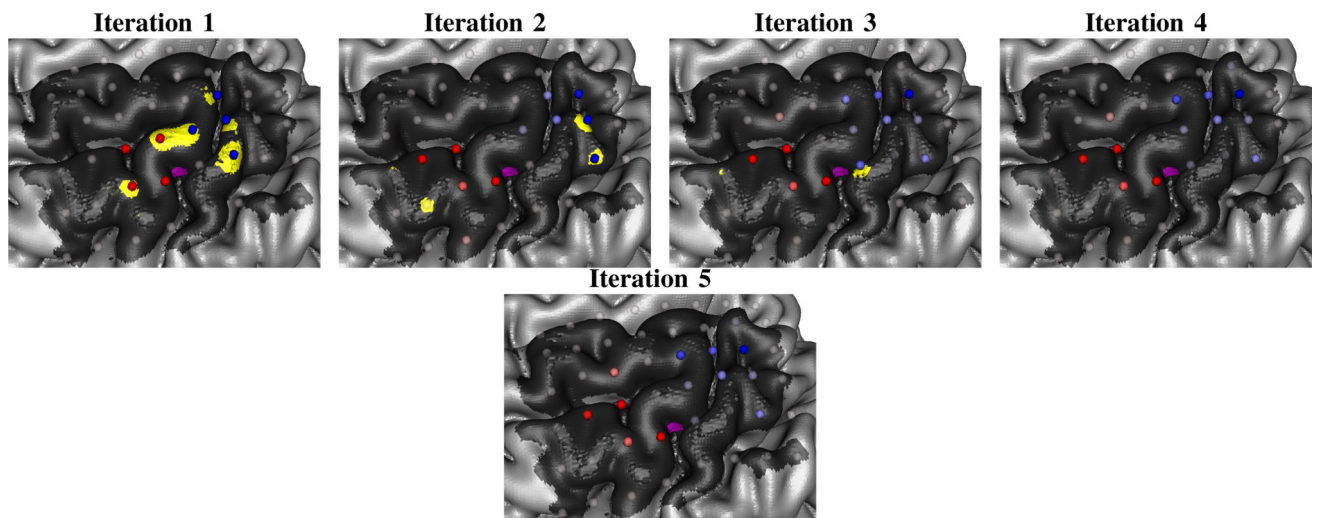


Fig. B.9.

Optimization results for ROI 4, tangential direction.

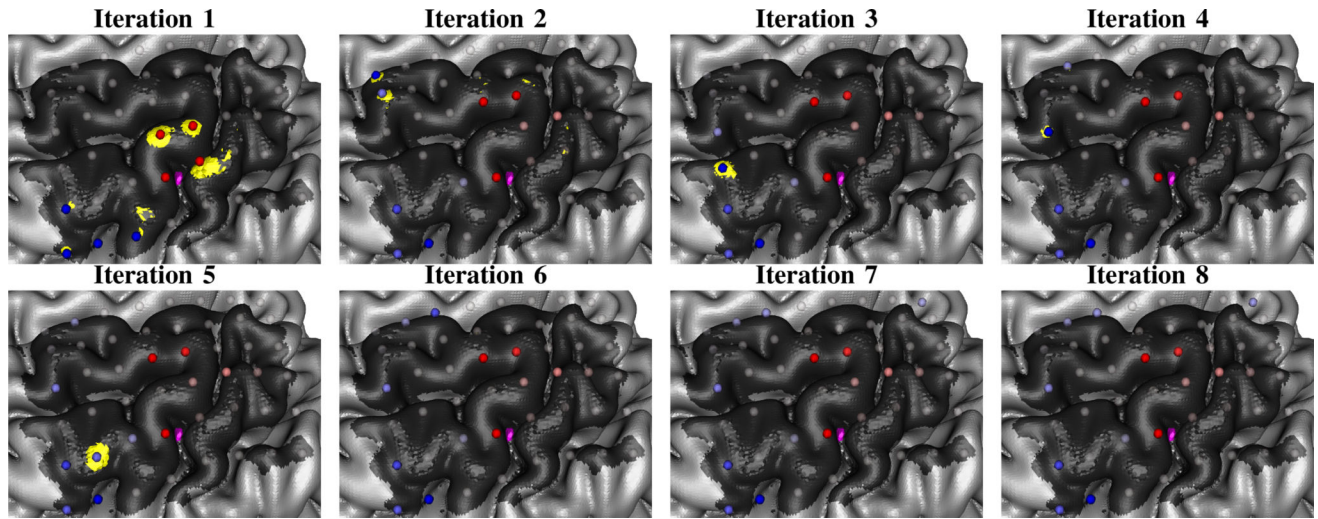
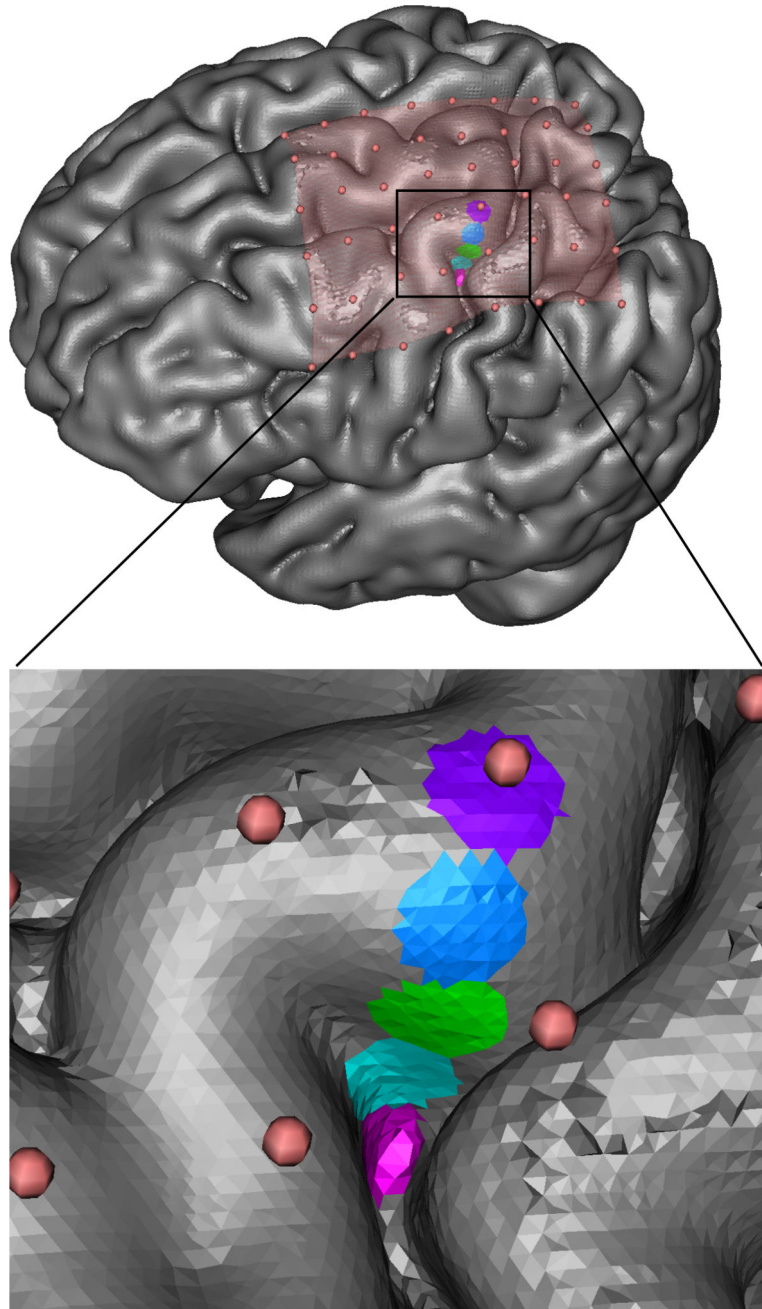


Fig. B.10.

Optimization results for ROI 5, in tangential direction.

**Fig. 1.**

Brain surface tessellation of the realistic head model used in the simulations. (Top) the placement of the 6×8 ECoG grid over the cortical surface, including five ROIs (ROI 1—purple, ROI 2—blue, ROI 3—green, ROI 4—cyan, and ROI 5—pink) shown beneath the grid, and (bottom) a zoomed-in view of the five ROIs to highlight their locations relative to the closest electrodes on the grid. The ECoG sheet is shown with transparent salmon on the top panel and the point electrodes are represented with salmon spheres on both panels.

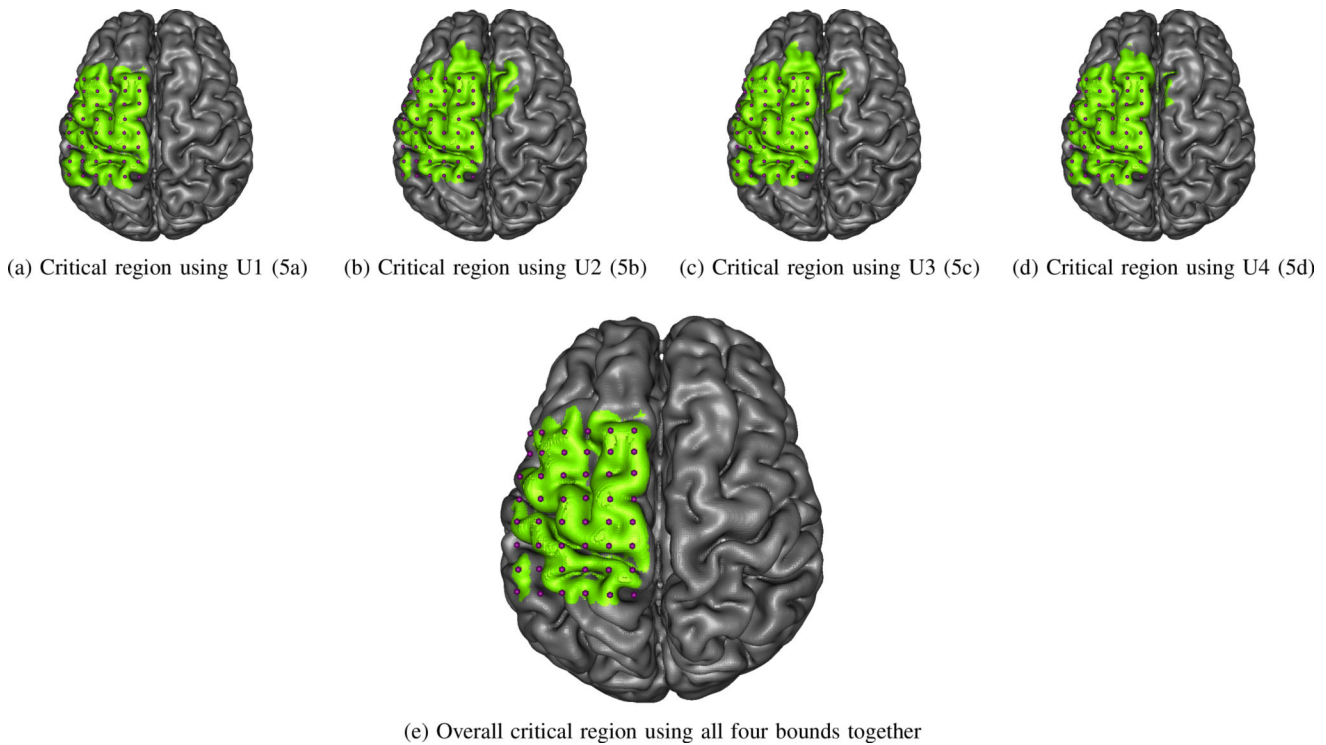
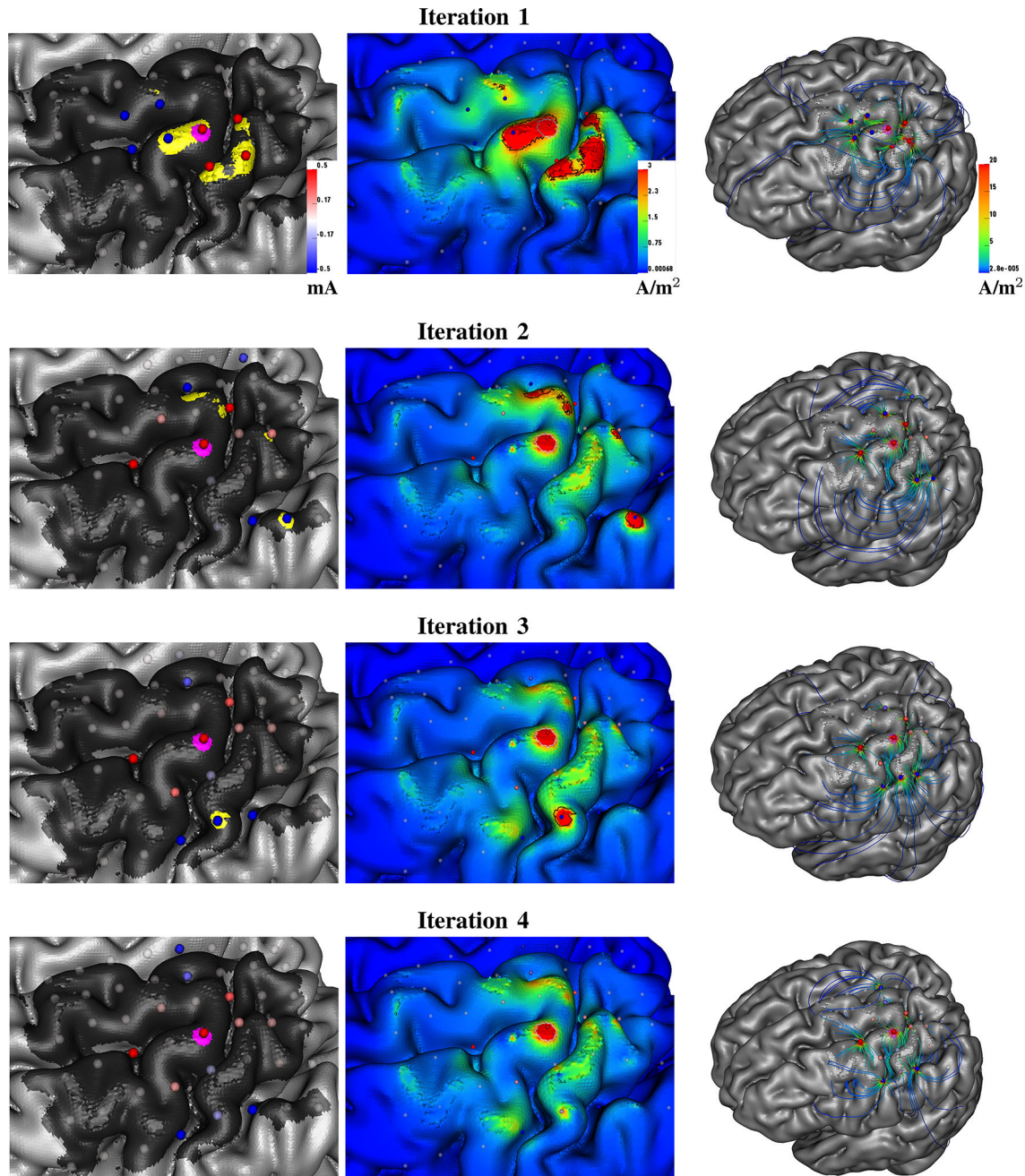


Fig. 2.

Critical (green) and safe (gray) regions of the cortical surface with a safety threshold of 2.5 A/m^2 , based only on the four upper bounds U_{1-4} in (5), given the total injected current is bounded by 2 mA and individual electrode currents by 0.5 mA. Purple dots show ECoG electrode locations. Overall critical region in the bottom panel comprises elements not guaranteed to be safe by any of the four upper bounds U_{1-4} .

**Fig. 3.**

Optimization results for gyral ROI and radial desired directional field, with each row showing results for one iteration. (Left) optimal stimulus pattern, as well as the critical region (dark gray), ROI (purple), and hot-spots (yellow). (Middle) the current density magnitude on the cortical surface, with hot-spots highlighted with black contours and ROI highlighted with a thin white contour. (Right) current streamlines through the brain tissue. As stated above the current shunted through the CSF is not shown to prevent visual clutter. The colorbars on the top row are shared across rows.

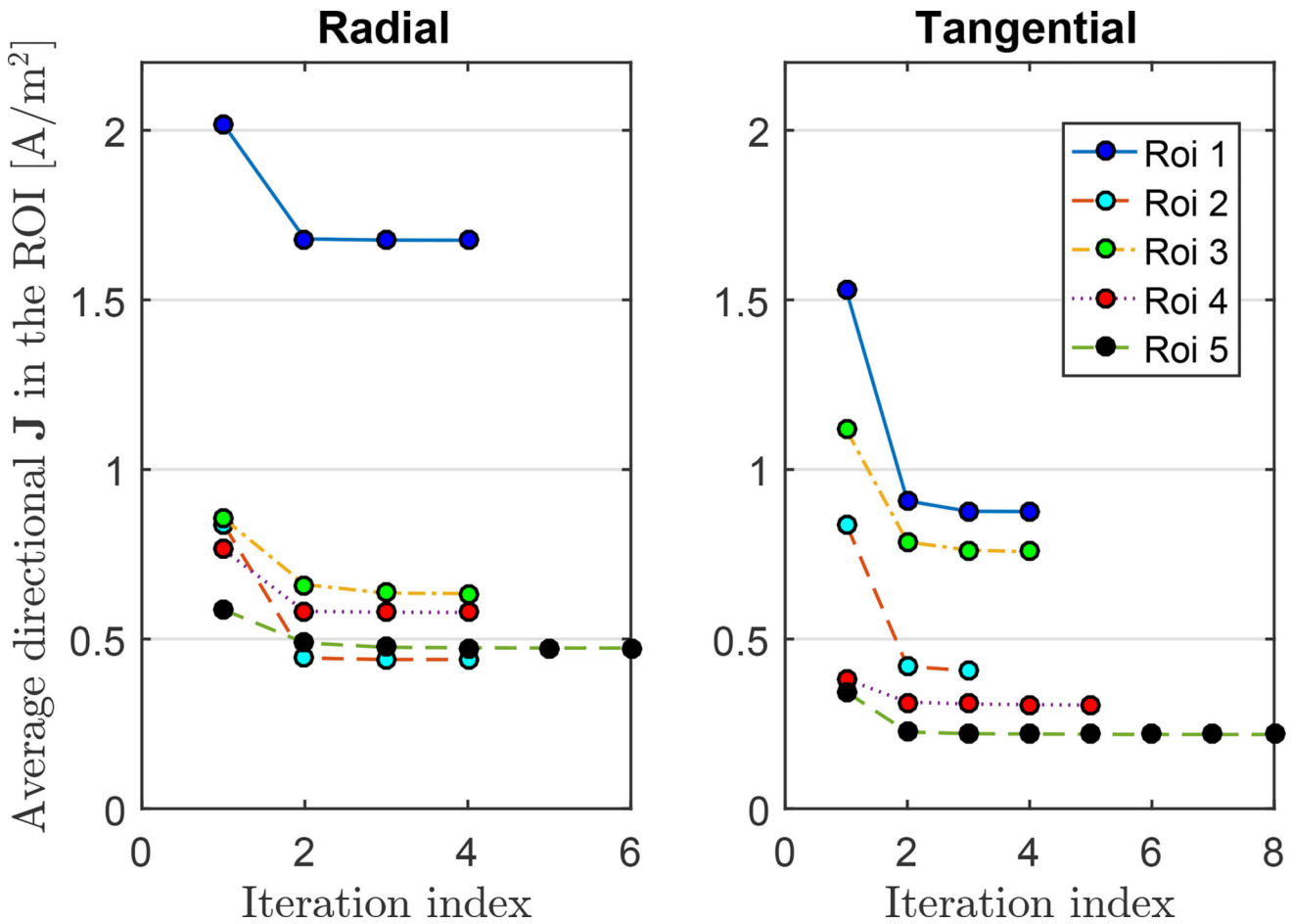


Fig. 4.

Average current density along the desired directional field in the ROI, for all five ROIs.

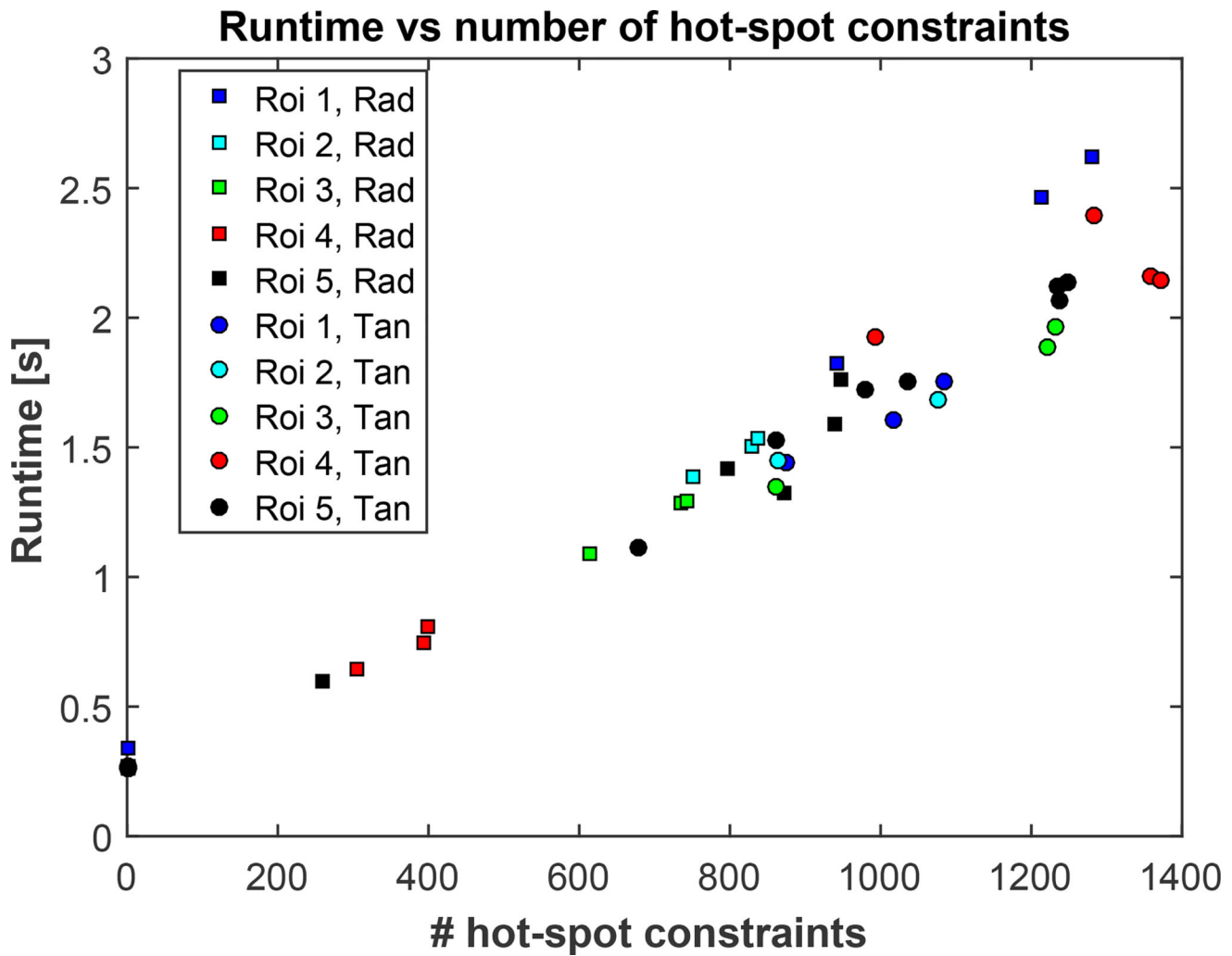


Fig. 5.
Runtime versus the number of hot-spot constraints at each iteration.

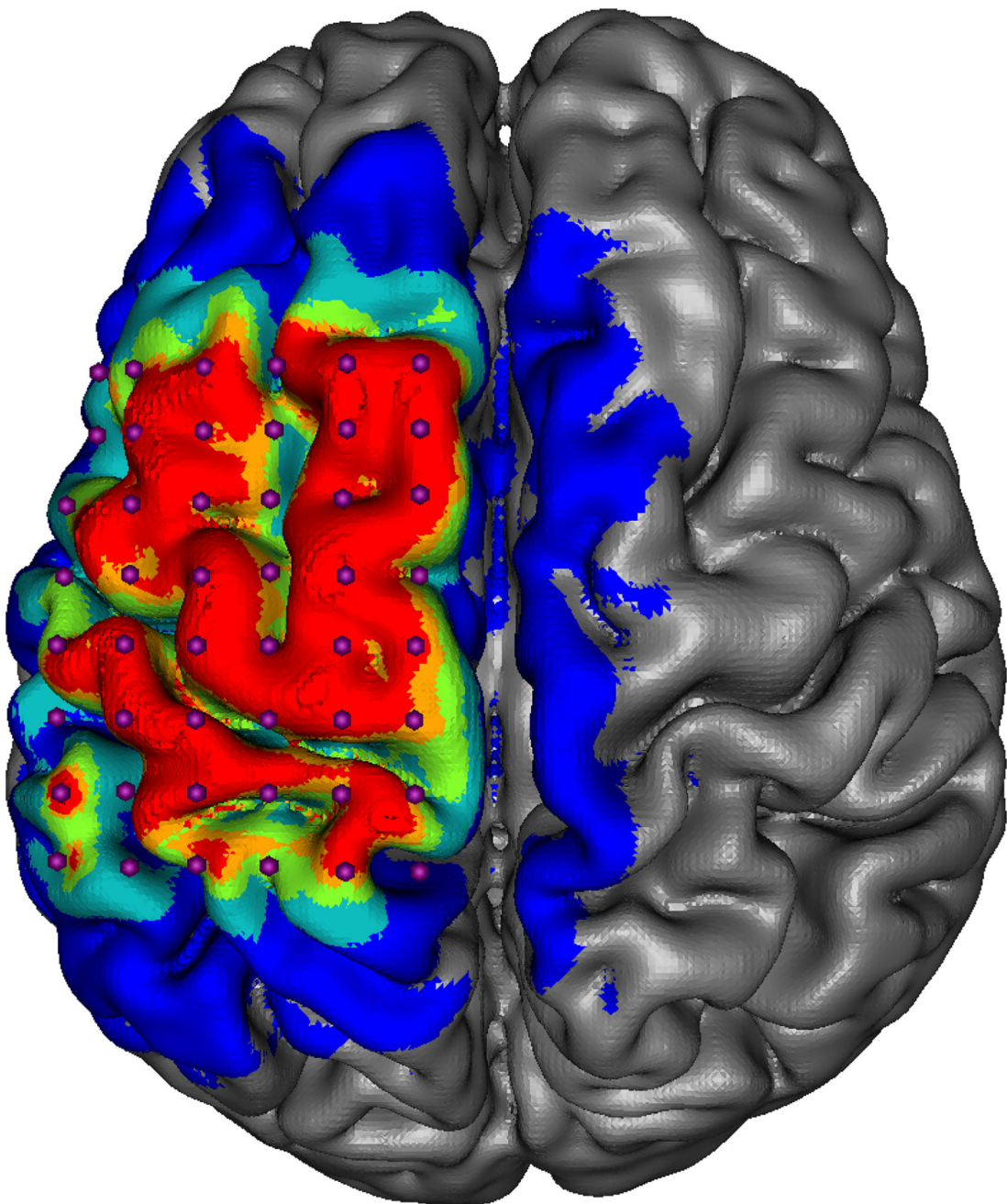


Fig. 6.

Critical regions for five different threshold values for the current density magnitude. The chosen threshold values were 4.5 (red), 3.5 (orange), 2.5 (green), 1.5 (light blue), and 0.5 (A/m^2).

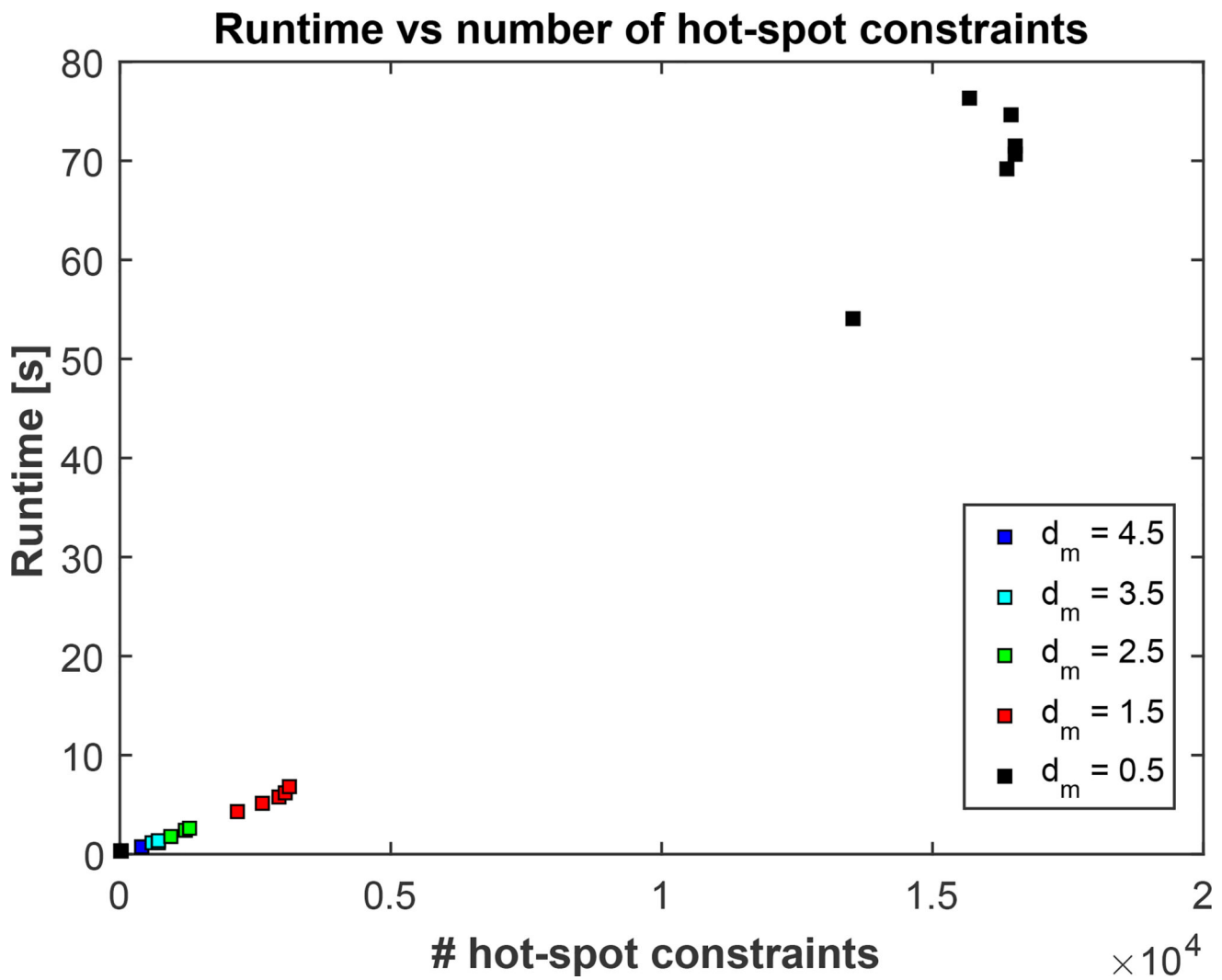


Fig. 7.

Runtime versus the number of hot-spot constraints at each iteration, for gyral ROI and radial desired directional field.

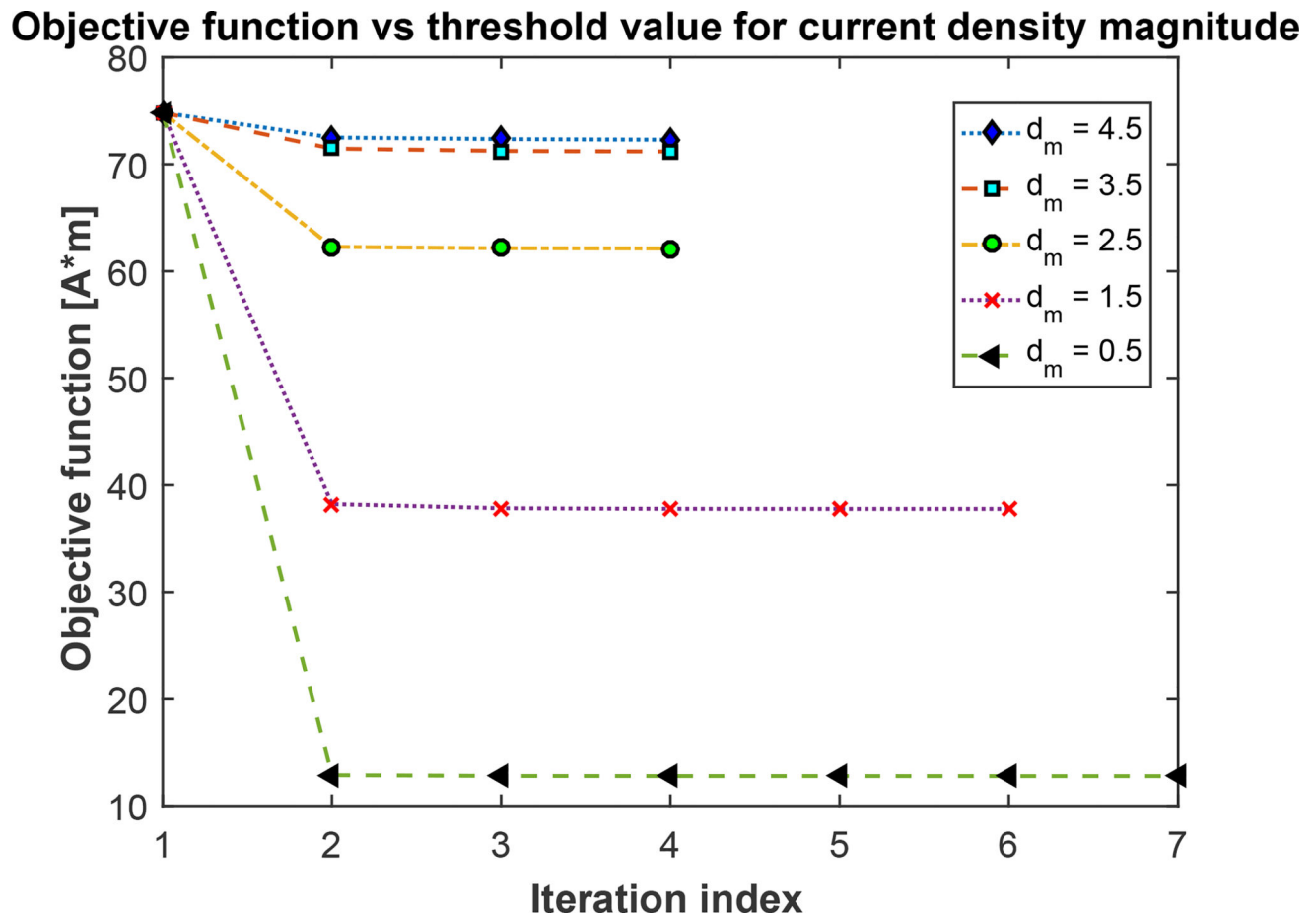


Fig. 8.

Objective function value at each iteration for different threshold values for hot-spots, for gyral ROI and radial desired directional field.

TABLE I

Notation for algorithm 1

C	A subset of constraints in (4)
$OP(C)$	Optimization problem with the objective (1), and constraints (2), with hot-spot constraints only on set C
H	Violated hot-spot constraints

TABLE II

Percentage of brain volume jointly and uniquely identified as safe by each upper bound.

Overall safe region (%)	Safe region uniquely identified by each bound(%)			
	U1	U2	U3	U4
97.10	0.73	0.30	0	0.03

Optimal average current density along the desired directional field in the ROI

Desired direction	Average directional current density (A/m^2)				
	ROI 1	ROI 2	ROI 3	ROI 4	ROI 5
Radial	1.68	0.44	0.63	0.58	0.47
Tangential	0.88	0.41	0.76	0.31	0.22

TABLE III